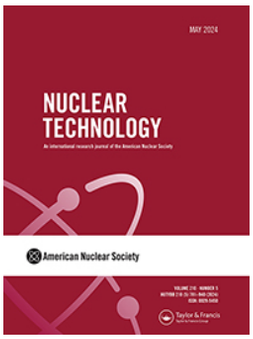

Nuclear Technology

ISSN: (Print) (Online) Journal homepage: www.tandfonline.com/journals/unct20

Modified Evaporation Model for ATHLET System Code in a Passive Containment Cooling System for Nuclear Safety

Michel Haag, Iurii Dolganov & Stephan Leyer

To cite this article: Michel Haag, Iurii Dolganov & Stephan Leyer (08 Apr 2024): Modified Evaporation Model for ATHLET System Code in a Passive Containment Cooling System for Nuclear Safety, Nuclear Technology, DOI: 10.1080/00295450.2024.2319933

To link to this article: https://doi.org/10.1080/00295450.2024.2319933

Published online: 08 Apr 2024.

NUCLEAR TECHNOLOGY

DOI: https://doi.org/10.1080/00295450.2024.2319933

Modified Evaporation Model for ATHLET System Code in a Passive Containment Cooling System for Nuclear Safety

Michel Haag, Iurii Dolganov,* and Stephan Leyer

University of Luxembourg, Campus Kirchberg, Faculty of Science, Technology and Medicine, Department of Engineering, 6, Rue Richard Coudenhove-Kalergi, Kirchberg L-1359, Luxembourg

Received May 23, 2023
Accepted for Publication February 10, 2024

Abstract — *The presented work deals with the improvement of the evaporation model of the ATHLET (Analysis of Thermal and Hydraulics of Leaks and Transients) system code to be applied to a passive containment cooling system of a nuclear power plant. For the model validation, INTRAVIT (Investigation of Passive Heat Transfer in a Variably Inclined Tube) test facility setup at the University of Luxembourg was used. The first part of the paper presents a review of the existing literature on evaporation models that revealed that those models significantly simplify the physical processes that occur. Next, a modified evaporation model is proposed that offers a realistic description of various evaporation processes and the start of bubble formation using a nucleation model, and a surface density calculation model is introduced that is necessary for evaporation simulation. The final part of this work explored five different system configurations to test the evaporation model: three condenser tube inclinations (5 deg, 60 deg, and 90 deg), two riser lengths (1 m and 2.5 m), and different thermal loads. They made it possible to simulate several experiments for stable and unstable natural circulation and to verify the proposed model.*

Keywords — *Natural circulation, two-phase flow, evaporation model, experimental data, nucleate boiling.*

Note — *Some figures may be in color only in the electronic version.*

I. INTRODUCTION

The ATHLET (Analysis of Thermal and Hydraulics of Leaks and Transients) system code was developed by the Society for Plant and Reactor Safety to analyze the behavior of nuclear power plants in the event of accidents. ATHLET consists of four modules that enable the coupling of thermal fluid dynamics (TFD), heat transport via structures (HECU), neutron kinetics, and the general control simulation module (GCSM). The focus here is on the TFD module. The local discretization of the computational network is based on a one-dimensional finite volume method in which the scalar quantities (pressure, temperatures, etc.) in the center of the cell and the vectorial quantities (velocities) at the cell edges are calculated. The six-equation model is used here for the mathematical description of the flow. A coupled explicit/implicit Euler method is used to solve the differential equation system. This determines the adaptive temporal discretization.[1]

The standard evaporation model in ATHLET contains various major simplifications to describe the evaporation

*E-mail: iurii.dolganov@uni.lu

process. In addition, in the ATHLET system code, a total of 13 setting parameters needs to be specified for the evaporation model. Among other things, these parameters, such as the number of bubbles/droplets per unit volume or relative bubble velocity, are difficult to set for the user and may contaminate the calculation results when chosen inappropriately. The critical simplifications and assumptions in modeling the evaporations can be listed as follows:

1. Use of minimum vapor content with subcooled liquid.
2. Sole consideration of the bubble and mist flow forms.
3. Calculation of droplet evaporation and bubble evaporation with the same Nusselt correlation.
4. Application of the thermal bubble growth over the entire flow range,[2] which can only be used for stagnant liquid phases.
5. No surface density calculation.

The modified evaporation model for ATHLET addresses the before mentioned simplifications. The main advantages of the modified evaporation model compared to the standard model are as follows: (1) division of flow into flow shapes: bubble flow, plug flow, churn flow, annular flow, and mist flow; (2) modeling of surface density depending on flow regimes; (3) use of the bubble nucleation model; and (4) modeling of heat transfer depending on the flow pattern (bubble growth/Nusselt correlation model).

II. LITERATURE REVIEW

Two theories of vapor bubble nucleation are widely known in the literature: homogeneous and heterogeneous. Homogeneous nucleation is defined as nucleation in a volatile phase that is not in contact with the vapor phase and completely wets all surfaces in contact (ideally smooth wall: contact angle of 0 deg).[3] However, heterogeneous nucleation can only take place if the contact angle of the volatile liquid is greater than zero.

II.A. Homogeneous Nucleation

The classical theory of homogeneous nucleation is based on the kinetic theory of heat.[4] It is assumed that the energy is unevenly distributed among the liquid-phase molecules. With such an energy distribution, there must be molecules that have a higher-than-average energy content. This access energy of the molecules is called the activation energy. Nucleation occurs when the density of the activated molecules is high enough to provide sufficient activation energy for nucleation. A collection of activated molecules is called an active cluster. As soon as an active cluster exceeds the critical radius r_c, this cluster can no longer collapse and is then referred to as a vapor nucleus.

From classical nucleation theory, several authors have based their work on this theory. Different approaches for calculating the nucleation rate and the maximum superheat can be found in the work of Blander and Katz[3] and Cole.[5] Due to the vanishingly small exponential term of the classical theory, meaningful nucleation rates can only be calculated for very high pressures and overheating. The classical theory is applicable to water only for $P < 0.5P_c$.[6] This thesis is also confirmed by Miller.[7] He made optical observations of a flashing flow in an adiabatic convergent-divergent nozzle. Experiments were examined under different flow conditions. In this work, no bubble formation was observed in the flow core. All bubbles formed on the nozzle wall.

II.B. Heterogeneous Nucleation

In technically relevant systems, the assumption of ideal smooth walls is not correct. Common machined surfaces have cavities on the order of 2 to 6 μm and a density of 10×10^4 to 250×10^4 m^{-2}.[8] Different cases can be distinguished in the case of heterogeneous nucleation. On the one hand, whether the wall is heated or adiabatic, and on the other hand, whether the liquid phase is stagnant (container boiling) or flowing (flow boiling). Section II.B describes the mechanism for heterogeneous nucleation in steps (a) through (d) (see Figs. 1a through 1d). A distinction is made between an adiabatic (Fig. 1e) and a heated wall (Fig. 1f).

Most heterogeneous nucleation theories are based on heated wall nucleation. Related theories have been derived for stagnant liquid on a horizontal heated plate (container boiling).

Reference[9] postulates that the derivation of nucleation on heated walls can also be used for boiling on adiabatic walls (flashing). The difference is in the definition of overheating. In flow boiling, the wall superheat fluctuates between $T_W - T`$ and 0 K due to the disruption of the temperature boundary layer caused by the bubble's formation. For superheat in volume or flow boiling, a mean superheat of $\Delta T_{sup.BL} = (T_W - T`)/2$ is used. In the case of flashing, there is no temperature boundary layer because of the adiabatic wall. Therefore, Ref. [9] proposed an overheating of $\Delta T_{sup.fls} = T_f - T`$ for nucleation during flashing.

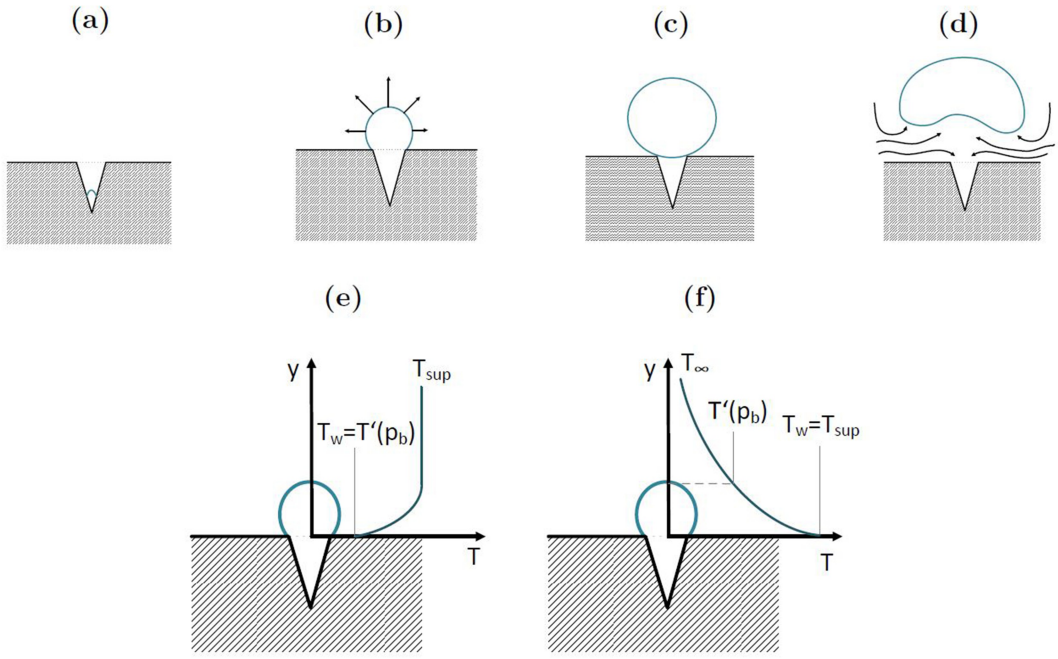

Fig. 1. (a) to (d) Mechanism of heterogeneous nucleation. Temperature boundary layer for nucleation with (e) adiabatic wall and (f) heated wall.

II.C. Flow Patterns

After the bubbles have formed and lifted off the pipe wall, they are moving in the bulk of the core flow. Various scenarios are possible here, such as

1. $T_f > T`$: the bubble continues to grow in the superheated flow.
2. $T_f = T`$: the vapor mass in the bubble remains constant, the bubble surface can deform due to the flow.
3. $T_f < T`$: the bubble condenses.
4. A large bubble can break up into several small bubbles (break up).
5. Several individual bubbles can collide and form a larger bubble or vapor area (coalescence).

Depending on the flow conditions and vapor content, the two-phase flow can exist in different flow forms. Figure 2 shows different flow patterns for vertical pipe flows.

If the vapor content is low, there is a bubbly flow (Fig. 2a). This generally has a higher phase velocity than the liquid phase. Depending on the size and relative speed of the bubbles, they can be spherical or elliptical.

At higher vapor content, the bubbles coalesce into larger cylindrical plugs (Taylor bubbles) that characterize plug flow (Fig. 2b). There is a film of liquid between the pipe wall and the stopper in which small bubbles can be

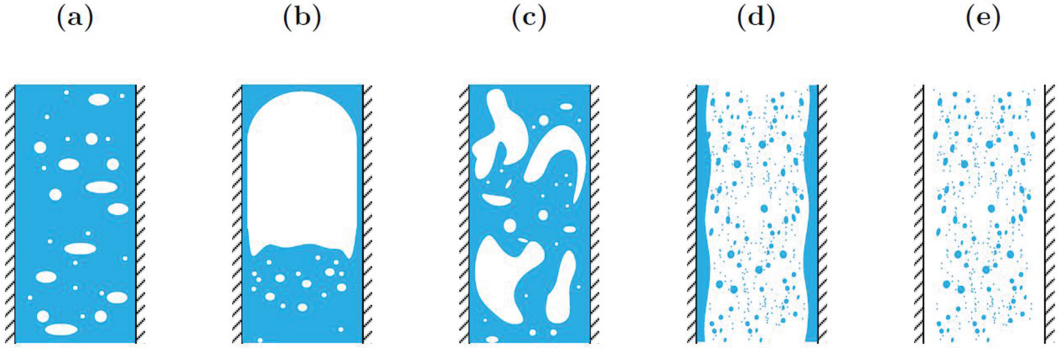

Fig. 2. Flow patterns of a vertical two-phase flow: (a) bubble flow, (b) plug flow, (c) foam flow, (d) ring flow, and (e) mist flow.

trapped. In the liquid phase between two vapor plugs there are often bubbles.

The churn flow (Fig. 2c) is a highly chaotic flow in which larger amounts of vapor bubbles detach from the tail of the Taylor bubbles and form larger vapor areas that are unstable. Churn flow is often avoided in technical two-phase systems since pressure and flow oscillations occur here.

Annular flow (Fig. 2d) consists of a higher velocity vapor core flow surrounded by an annular film. Due to shear stresses between the core flow and the film, waves can form on the film surface from which droplets can be detached, which then flow into the core flow and accumulate. The annular flow is desirable at the exit from the heat exchanger since the heat transfer is high due to the wetting of the tube wall despite the high vapor content.

Once the wall film has reached a critical thickness, it becomes unstable and dryout occurs. In the resulting fog flow (Fig. 2e), the remaining liquid phase is in the form of small droplets in the core flow.[10]

This classification of flow patterns is important because it can be used to make statements about the phase interface.

III. MATERIAL AND METHODS

III.A. Development of a Modified Evaporation Model

III.A.1. Flow Map for the Standard Evaporation Model

In the standard ATHLET model, a distinction is made between evaporation on heated surfaces and evaporation in the core flow. In this work, the focus is on the latter. ATHLET differentiates between two extreme cases when it comes to evaporation: evaporation with a low vapor content (bubble flow) and evaporation with a high vapor content (mist flow). Linear interpolation is used between them (Fig. 3).

When the vapor content is low, the evaporation model assumes that the flow consists of several spherical vapor bubbles with the same radius. A distinction is made between bubbles with and without relative velocity to the liquid phase.

In case the bubble moves with the same velocity as the liquid phase ($W_{rel} = 0$), the starting point for the description of the evaporation is the thermal bubble growth model.[2]

III.A.2. Flow Map for the Modified Evaporation Model

A flow map has the benefit of dividing the flow into different flow regimes depending on one or more parameters. Knowledge of the flow regime is important since most models are only applicable to a specific regime.

Many flow maps classify the flow regimes depending on the velocities for the gas and liquid phases. Since the flow patterns are geometric parameters, such parameters (e.g., volume vapor content or surface density) should also be used as parameters for classification. A direct connection between the superficial velocities and the gas content could exist only in the case of a steady flow. For strong transient flows and flows with reverse flow, the conventional formulation in combination with the six-equation model used here may not be sufficient. It is proposed to use a flow map that depends directly on the vapor content.[11]

The flow map applied here therefore divides the flow into three areas depending on the volume vapor content: nucleation bubble flow, plug and churn flow, and annular/mist flow. There is a narrow interpolation area between the different areas in order to avoid discontinuities that lead to numerical instabilities. Figure 4 shows the flow map used for the modified evaporation model.

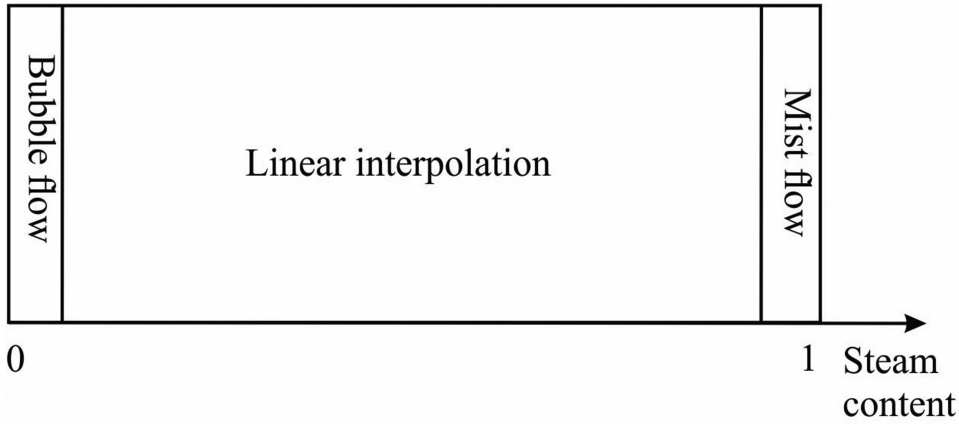

Fig. 3. Flow map for standard evaporation model.

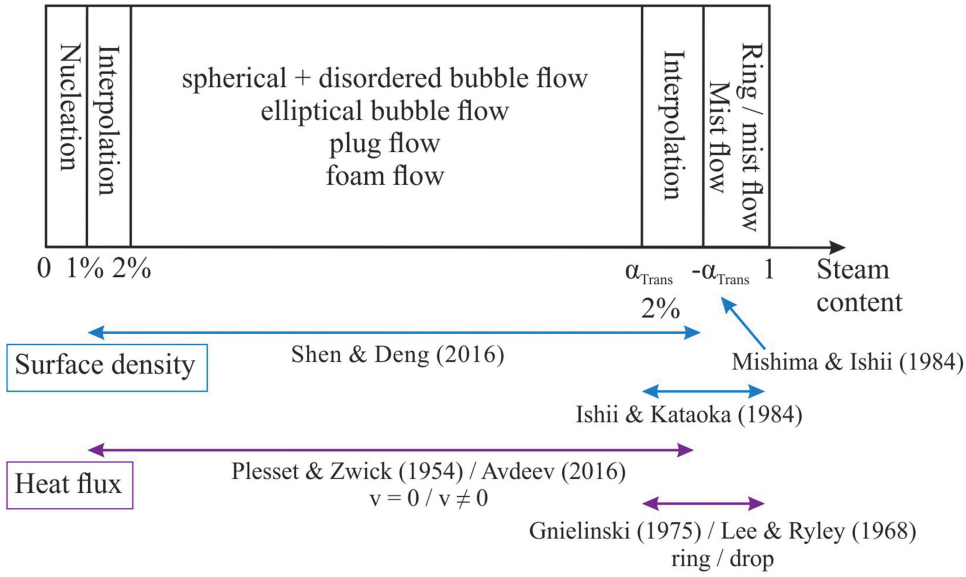

Fig. 4. Flow map for modified evaporation model.

III.A.3. Nucleation Model

Three parameters must be modeled to calculate the formation of vapor through nucleation: r_{det}, n_{ns}, and f_{det}.

The detachment radius r_{det} is the bubble radius from which the bubble has reached the size from which it detaches from the cavity. Because of better agreement with the experimental data, the model by Shin and Jones[12] was used to calculate the detachment radius,

$$r_{det} = K\sqrt{\frac{4\sigma R_{crit}}{C_d \rho_f w_{BL}^2}} \tag{1}$$

where C_d is the drag coefficient, w_{BL} is the flow velocity in the boundary layer, and K is the pre-factor that takes into account the portion of the capillary force that counteracts the drag force.

Because of the problem described previously that the model from Shin and Jones[12] cannot be used at low flow velocities because of the vanishing wall shear stress, the model from was considered for this range,

$$r_{det} = \theta\left[\frac{\sigma}{g\left(\rho_f - \rho_{st}\right)}\right]^{1/2} Ja \quad . \tag{2}$$

Finally, the minimum of both models was taken for the detachment radius in order to avoid numerical instabilities in the transition from one model to the other.

The experimental data in the work of Basu et al.[13] and the complementary correlation in Ref. [14] allow us to add in the model a numerical expression for determining the number of nucleation sites N_{ks},

$$n_{ns} = \overline{n_{ns}}\left[1 - exp\left(-\frac{\theta}{8\mu^2}\right)\right]\left[exp\left(f(\rho^+)\frac{\lambda'}{r_k}\right)\right] \quad . \tag{3}$$

The average number of wall nucleation sites $\overline{n_{ns}} = 4.72 \cdot 10^5$ and the statistical parameter $\lambda` = 2.5 \cdot 10^{-6}$ m were determined by Basu et al.[13] $\mu = 0.722$ rad is another static parameter and can be considered as the characteristic angle of the cone of the cavity ($\rho^+ = \log(\Delta\rho/\rho_g)$) and $r_k^+$ is the dimensionless critical radius of a cavity ($r_k^+ = r_k/\lambda`$). $f(\rho^+)$ is a function of the dimensionless logarithmic density difference (used as a correction function),

$$f(\rho^+) = -0.01064 + 0.48346\rho^+ - 0.22712\rho^{+2}$$

$$+0.05468\rho^{+3} \quad . \tag{4}$$

The detachment frequency f_{det} is the frequency with which a bubble with the detachment diameter d_{det} detaches from a cavity. The work of Riznic and Ishii[9] showed good convergence results using the Zuber[15] model,

$$f_{det} = \frac{1.18}{2d_{det}}\left[\frac{\sigma g\left(\rho_f - \rho_{st}\right)}{\rho_f^2}\right]^{1/4} \quad . \tag{5}$$

III.A.4. Annular and Mist Flow

The basic idea for calculating surface flux density in an annular/mist flow is based on the work of Ishii and Kataoka.[16] The surface density of the annular flow is determined separately from the density of the mist flow, so four different cases can occur:

1. *Clean annular flow*: liquid film on the wall.
2. *Annular/mist flow*: film of liquid on the wall and droplets in the main flow.
3. *Pure mist stream*: only drops in the main stream.
4. *Clean steam flow*: without liquid content.

To determine the entrainment factor, the empirical entrainment model[17] was used here, which depends only on the Weber number of the core flow W_{ek}. The surface density of the annular flow required to determine the Weber number can be calculated using the following formula:

$$A_i = \frac{4}{d_h}\sqrt{\frac{\varepsilon}{1-\varepsilon_d}} f_{rdc} f_{wav} \quad . \tag{6}$$

where the first quotient $4/d_h$ describes the surface density of the tube wall, the root term $\sqrt{\frac{\varepsilon}{1-\varepsilon_{st}}}$ increases the surface density because of the reduced core diameter d_k due to the film thickness, the f_{rdc} factor reduces the surface density as soon as the film begins to dryout and only partially wets the pipe wall, and f_{wav} is used to account for the increased surface density due to film waviness.

The critical film thickness at which the wall film dryout and rivulets form was calculated using the empirical correlation[18]

$$\delta_{crit} = \frac{(1-cos(\theta_0))^{0.22}}{\left(\frac{\rho_f^3 g^2}{15\mu_f^2\sigma}\right)^{0.2}} \quad . \tag{7}$$

The wall film thickness was calculated from the difference between the hydraulic diameter d_h and the main flow diameter d_k,

$$\delta = \frac{d_h}{2}\left(1-\sqrt{\frac{\alpha}{1-\alpha_{st}}}\right) \quad . \tag{8}$$

III.A.5. Transition Between Churn and Annular Flow

The transition from churn flow to annular flow is not a fixed limit, but depends, among other things, on the system pressure and the phase velocities. For this reason, it makes sense to use a model to determine the transition area. The model of Mishima and Ishii[11] was suitable for this. The critical steam content, from which the transition from the churn to the annular flow begins, is determined from the minimum of two criteria,

$$\varepsilon_{crit} = min(\varepsilon_{c1}, \varepsilon_{c2}) \quad . \tag{9}$$

In churn flow, the flow direction of the film between a large bubble and the tube wall is opposite to the flow direction of the bubble. When there is a flow reversal of the film, the liquid phase is sucked from the core flow into the film. From this assumption, a first transition criterion for the superficial velocity is established as

$$Jd_{crit1} = \sqrt{\left(\frac{\Delta\rho g D}{\rho_g}\right)(\varepsilon - 0.11)} \quad . \tag{10}$$

The second mechanism states that the transition occurs as soon as detachment (entrainment) from the wall film begins. It is assumed that the detached droplets fly through the phase boundary layer of large bubbles at high speed, destroying them in the process. Entrainment begins when the criterion is satisfied,

$$Jd_{rit2} = \left(\frac{\sigma g \Delta\rho}{\rho_{st}^2}\right)^{1/4} N_{\mu f}^{-0.2} \tag{11}$$

$$N_{\mu f} = \frac{\mu_f}{\left[\rho_f \sigma \sqrt{\frac{\sigma}{g\Delta\rho}}\right]^{1/2}} \quad . \tag{12}$$

In this work, the flow map was based on the volumetric vapor content and not on the superficial velocities. Therefore, the critical vapor velocities described previously must be converted into critical volumetric vapor contents. With the definition of the superficial velocity

$$Jd = \varepsilon \frac{\dot{m}}{\rho_{av} A_h} \tag{13}$$

together with the average density

$$\rho_m = \varepsilon\rho_v + (1-\varepsilon)\rho_1 \quad , \tag{14}$$

the critical steam content for fulfilling the second transition criterion can be calculated as

$$\varepsilon_{c1/2} = \frac{-\rho_f}{\rho_{st} - \rho_f - \frac{\dot{m}}{A_h J d_{crit1/2}}} \quad . \tag{15}$$

Pressure has a great influence on the critical transient steam volume content. From this we can conclude that it makes sense to simulate the transition point and not to set a fixed critical steam content.

III.A.6. Interpolation Areas

Two interpolation areas are shown in the flow map (see Fig. 4). In these areas, both the surface density and the heat flux models overlap. The interpolation creates a continuous transition between the two functions. The width of the interpolation regions is 1% between nucleation and bubble flow and 2% between churn flow and annular flow. This work uses the method of logarithmic interpolation as it approaches the target value of the function faster,

$$y = y_1^{(1-f)} \cdot y_2^f \quad . \tag{16}$$

Figure 5 shows the surface density from the two-group model, the annular flow,[16] and the critical transition vapor content,[11] and the course of the total surface density resulting from the interpolation is shown for two different mass flows. The second interpolation limit is at the point where the transition model predicts the transition to annular flow. The first interpolation limit is at a vapor content that is 2% lower.

III.A.7. Heat Flux

III.A.7.a. Bubble Flow

For the evaporation of the bubble flow, a distinction is made between turbulent and laminar pipe flow. For laminar and stagnant pipe flow, the evaporation is described using a bubble growth model.

In this work, the model of Plesset and Zwick,[2] based on the theory of thermally limited bubble growth, was used. This model showed good results with the experiments of Dergarabedian[19] carried out with stagnant liquid. Thus, the use model of Plesset and Zwick[2] was also justified for a stagnant liquid phase, despite the relative velocity between the phases. Bubble growth is written as[2]

$$\frac{dr}{dt} = \frac{1}{2} Ja \sqrt{\frac{12 a_f}{\pi}} \frac{1}{\sqrt{t}} \quad . \tag{17}$$

For turbulent flow, the semi-empirical model of Avdeev,[20] based on the "surface renewal and penetration" approach, was used. The following Nusselt correlation was obtained:

$$\mathrm{Nu} = 0.23 \mathrm{Re}^{0.7} \mathrm{Pr}^{0.5} A^{0.25} \qquad \mathrm{Re} > 10^4$$

$$\mathrm{Nu} = 2.3 \mathrm{Re}^{0.45} \mathrm{Pr}^{0.5} \left(\frac{\rho_f}{\rho_m} \right)^{0.45} \qquad \mathrm{Re} \leq 10^4 \tag{18}$$

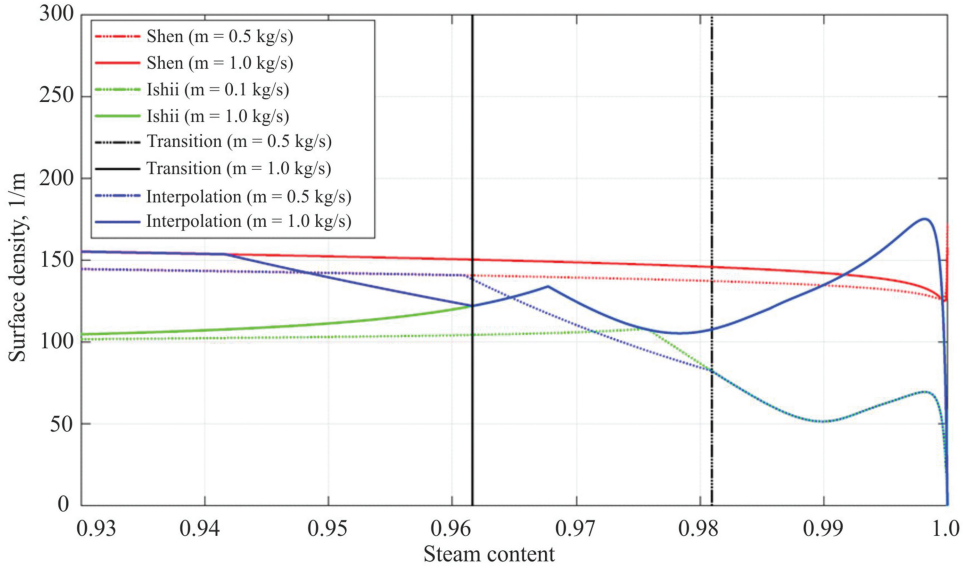

Fig. 5. Representation of interpolation range between two-group model and model for annular flow for two different mass flows ($\dot{m}$ = 0.5 kg/s and $\dot{m}$ = 1.0 kg/s). Vertical line represents transition from foam to ring flow.

where

$$A = \frac{1}{1-\varepsilon}\left(\frac{\rho_l}{\rho_m}\right)^{2.53} \quad . \tag{19}$$

III.A.7.b. Plug and Churn Flow

There are no model theories and experimental data in the literature for calculating the heat transfer coefficient in slug and churn flow. Due to the lack of correlations and the fact that slug and churn flow is highly turbulent, the Avdeev model[20] was also used here for this flow range [see Eq. (18)].

III.A.7.c. Annular/Mist Flow

To calculate the heat flow density in the annular/mist flow, the annular flow is considered separately from the mist flow.

Here it is assumed that the heat transfer between the core flow and the film behaves like the heat transfer from a single-phase pipe flow to the pipe wall. A widely used model for this,[21] which is used for turbulent pipe flows is

$$Nu = \frac{\xi/8\,(Re-1000)Pr}{1+12.7\sqrt{\xi/8}\left(Pr^{2/3}-1\right)} \tag{20}$$

with the drag coefficient

$$\xi = (1.82\log Re - 1.64)^{-2} \quad . \tag{21}$$

For the laminar case, the Nusselt number takes on a constant value as shown in Ref. [22],

$$Nu = 3.657 \quad . \tag{22}$$

The critical Reynolds number of 2300 was chosen for the division between turbulent and laminar flow. In the transition range (Re = 2300 to 3500), an interpolation is made between the laminar and the turbulent range. To calculate the Reynolds number, the steam velocity and the core flow diameter are used as a characteristic measure of length.

The heat transfer between the vapor phase and the mist flow is calculated according to the empirical model[23] in Eq. (23),

$$Nu = 2 + 0.74\mathrm{Re}^{0.5}\mathrm{Pr}^{0.33} \quad . \tag{23}$$

This model is based on optical experiments of an evaporating water droplet in a steam atmosphere, and therefore, was appropriate for this application.

III.B. Description of the ATHLET Model

For the modeling of the INTRAVIT experimental setup, the geometric dimensions of the system were transferred to ATHLET via the input data set. Figure 6 shows the discretization of the TFD and HECU objects. The basin was divided into two separate TFD objects. The subdivision

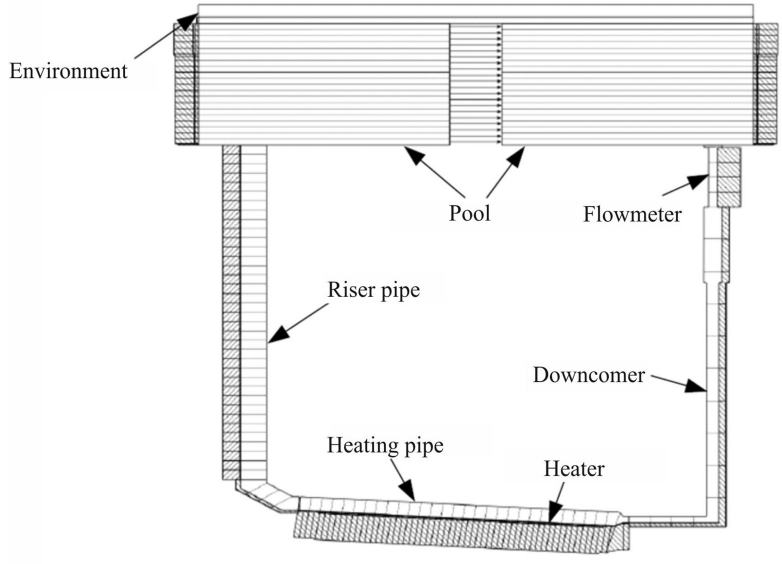

Fig. 6. Discretization of TFD and HECU objects (shown hatched) of INTRAVIT model with extended riser (not drawn to scale).

was needed because the six-equation model allows for only one flow direction per phase at the control volume boundary. In the case of a basin consisting of a single TFD object, the water could not flow from the riser into the lower control volume of the basin and at the same time flow out of it into the downcomer. In addition, temperature stratification in the basin would be prevented. Due to the subdivision of the basin, different flow directions of the liquid phase can occur on the respective sides. The two halves of the pool are connected via cross connections, which allow a mass flow perpendicular to the direction of flow. The top of the basin is connected to the ambient boundary condition (air: P = 1 bar) via a single control volume.

The remaining pipes are simple TFD objects. To model the thermal inertia of the system, the TFD objects were linked to the HECU objects via their perimeter. For this purpose, the wall thickness of the pipe, the insulation thickness, and the material data of the materials were considered. The outside of the insulation was assumed to be adiabatic. The mass flow meter, which is a comparatively heavy component, was also mapped with a corresponding HECU object. The filament was modeled as a separate HECU object with a homogeneous heat source located between the heater tube wall HECU object and the heater tube insulation.

The modeling of the temperature distribution in the pool, together with the idealized representation of an adiabatic downcomer, means that an accurate calculation of the heating pipe inlet temperature was not given. Since this temperature has a strong influence on the stability of the temperature at the system, it is important that the heater tube inlet agrees with the experimental data for later analysis. To eliminate this source of error in the model, a heat source was implemented in the downcomer.

The mass flow and the enthalpy in the downcomer were determined by means of a GCSM signal. The heat to be supplied, which is required to reach the target temperature, was calculated using a heat balance and fed in via the heat source. This ensured that the temperature at the heating tube inlet corresponded to the temperature profile specified by the user. The Martinelli-Nelson model was used to calculate the frictional pressure losses in the two-phase flow. The pressure losses, which were induced by the fittings, must be specified by the user using a pressure loss coefficient ζ.

Depending on the system configuration (different angles of inclination), the pressure loss changes so the pressure loss coefficients must be adjusted for each configuration. The heating power supplied must also be adapted to the experiments since, in contrast to the experiments, the model is an idealized adiabatic insulation.

The pressure loss coefficient and the heating capacity were adjusted in such a way that at a relative heating capacity of 100%, the mass flow and the riser inlet temperature agreed with the data from the experiments. The settings for the power supplied and the drag coefficients remained the same for each individual system configuration. Between the different simulations, only the pool temperature and the profile of the downcomer temperature were adjusted.

Backflow in the system code ATHLET can be simulated. The location of the mass flow meter (located in the downcomer) was not numerically predicted here. That does not mean that there may be a backflow in the riser tube. However, experimentally this cannot be unraveled.

All the submodels forming the nucleation mode do consider the gravity effect, and hence, the inclination is considered, which applies also to the conservation equations in ATHLET.

However, the calculated detachment radiuses of the bubbles are small compared to the pipe diameter, so the impact of the inclination of the pipe to bubble generation is not significant.

A total of four different system geometries were created in ATHLET: three with different inclination angles of the heating pipe (0 deg, 60 deg, and 90 deg) for measurement campaign 1 and one with the 2.5-m riser pipe from measurement campaign 2. For measurement campaign 2, simulations were carried out with three different chokes.

IV. RESULTS

IV.A. Simulation of Stable Natural Circulation

The results of the ATHLET simulations for the stable natural circulation are shown in Fig. 7 together with the experimental results for the inclination angles: 5 deg, 60 deg, and 90 deg. The upper row shows the mass flow in the downcomer, and the lower row shows the riser inlet temperature. As described previously, the pressure loss coefficients in the downcomer and the power supplied were adjusted in such a way that the results of the simulation matched those of the experiment as best as possible at the high heating power.

From Fig. 7 it can be seen that with the selected pressure loss coefficients, the simulation is in good agreement with the experiment even with the heating capacities of 60% and 80%. With heat outputs of 20% and 40%, the mass flow is underestimated and the riser pipe inlet

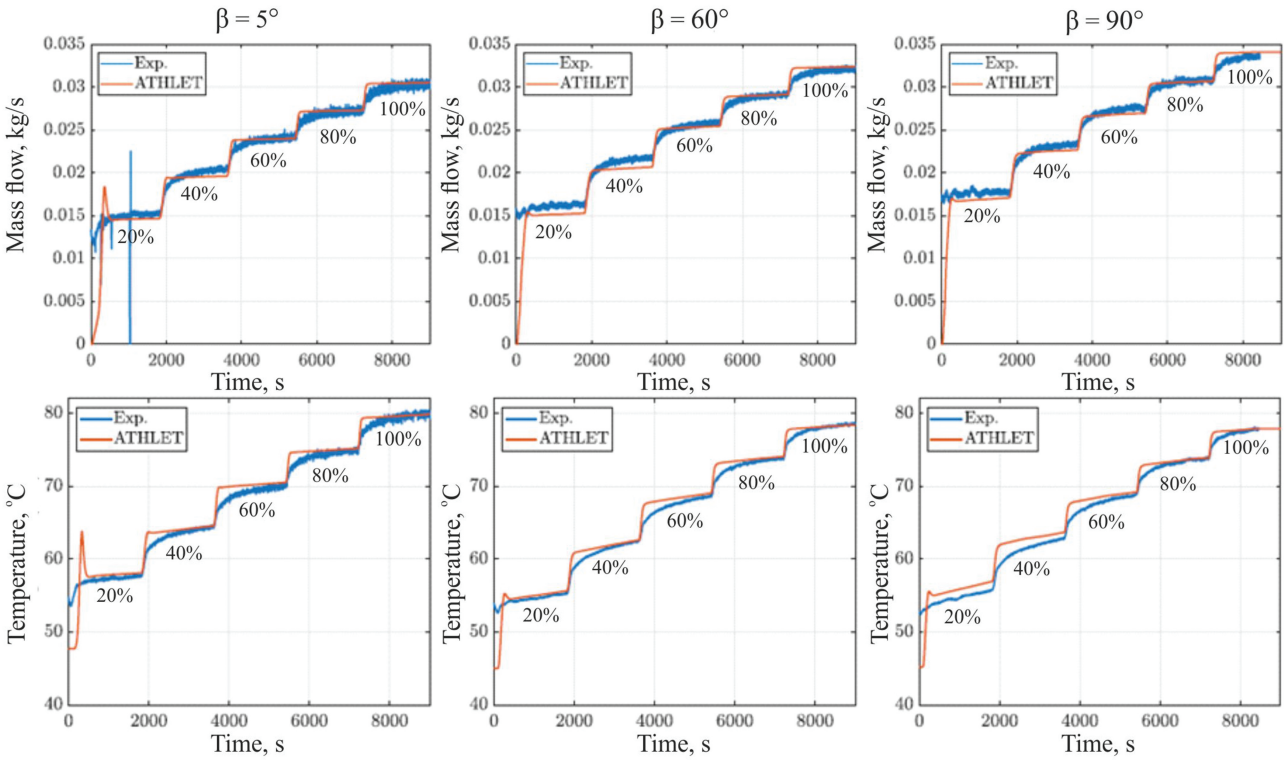

Fig. 7. Comparison of simulation results with the experimental data for the single-phase natural circulation with the inclination angles 5 deg, 60 deg, and 90 deg. Upper row shows mass flow in the downpipe, and lower row shows temperature in the riser pipe inlet.

temperature is overestimated. A reduction in the pressure loss coefficient would achieve the desired effect (higher mass flow and lower riser outlet temperature). However, such a change would worsen the simulation results at higher heating powers. Entering a flow rate–dependent pressure loss coefficient could help, but this is not intended in ATHLET. Instability occurs at powers greater than 80% where the error caused by low powers is not taken into account.

The simulation underestimates the transient range from the point at which the power increases until equilibrium is reached. Thus, the simulation reaches an equilibrium point much sooner. The transient range could be extended by adding thermal mass. This is not necessary here, since only the oscillations toward the end of the respective power levels are considered in the subsequent analysis of the instabilities.

Another difference between the simulation and experiment can be seen right at the beginning. Especially in the simulation with an inclination angle of 5 deg, a strong overshoot can be observed both in the mass flow and in the temperature curve.

This overshoot is due to the initial condition. During the test, the system was already in motion at the beginning, whereas the system was at rest during the simulation since the initial temperatures were the same everywhere. Only when the heating pipe heats up and inclines does the circulation slowly start to move, since at this point in time there is only a temperature difference within the heating pipe that can drive the system. The water in the heating pipe heats up more because the flow is initially slow. Once the warm water is in the riser, the circulation accelerates, leading to the overshoot. This effect is smaller, the greater the angle of inclination, since the greater the angle of inclination, the greater the driving force.

IV.B. Simulation of Unstable Natural Circulation

Based on the simulations of stable natural circulation, only the pool temperature and the course of the downcomer temperature were adjusted for the simulation of the unstable natural circulation. The rest of the settings remained unchanged. A total of nine operating points in the unstable range were simulated, five of them from measurement campaign 1 and four from measurement campaign 2. The simulation results with the standard model and those with the modified evaporation model were compared with the experimental data for the selected operating points.

TABLE I

Comparison of Simulation Results of Used Standard Evaporation Model and Modified Evaporation Model with Experimental Results

	f (mHz)			m'_{peak} (kg/s)			m' (kg/s)			
	Experi-mental Results	Standard	Modified	Experi-mental Results	Standard	Modified	Experi-mental Results	Standard	Modified	Inst.
Measurement Campaign 1 (1-m Riser Pipe)										
β5T85P80 relative error (%)	14.90	16.92 to 13.55	19.23 to 29.06	0.0966	0.1551 to 60.59	0.2015 to 108.68	0.04247	0.04258 to 0.25	0.04166 to 1.91	Flashing
β5T85100 relative error (%)	24.99	27.63 to 10.56	35.86 to 43.53	0.1213	0.1531 to 26.23	0.2581 to 112.88	0.05429	0.05735 to 5.6519	0.05349 to 1.47	Flashing
β60T85P80 relative error (%)	16.32	14.48 to 11.26	17.47 to 7.05	0.1367	0.1475 to 7.88	0.2048 to 49.77	0.04084	0.04131 to 1.16	0.04130 to 1.13	Flashing
β60T85P100 relative error (%)	41.02	32.56 to 20.64	34.45 to 16.02	0.1893	0.2298 to 21.38	0.2463 to 30.07	0.04782	0.05275 to 10.31	0.05317 to 11.20	Geysering
β90T85P100 relative error (%)	39.88	27.11 to 32.03	30.77 to 22.84	0.2101	0.1877 to 10.66	0.2324 to 10.62	0.04986	0.05436 to 9.04	0.05492 to 10.16	Geysering
Measurement Campaign 2 (2.5-m Riser Pipe)										
B09T85P100 relative error (%)	10.12	11.20 to 10.68	12.45 to 22.97	0.1713	0.2829 65.15	0.3076 to 79.55	0.05354	0.04996 to 6.69	0.04956 to 7.44	Flashing
B07T85P100 relative error (%)	35.11	28.17 to 19.78	29.72 to 15.35	0.1877	0.2212 17.84	0.2192 to 16.77	0.04007	0.04608 to 14.98	0.04093 to 2.13	Geysering

An overview of the simulation results for all simulated operating points is listed in Table I. The table shows selected parameters to describe the instabilities of the simulations and the experiment as well as their relative errors. The frequency of the maximum mass flow peaks, the average maximum mass flow peak, and the arithmetic mean over the mass flow are displayed as parameters. To calculate the arithmetic mean, the quotient of the integrated mass flow and the integration interval were formed. The tests from measurement campaign 2 without an aperture and with the 7-mm aperture at P_{rel} = 80% are not shown, since only one or two oscillations occurred with the instabilities, and therefore, no meaningful parameters could be determined.

Figure 8 shows the results of the second measurement campaign (rising pipe: 2.5 m, P_{rel} = 100%). The temperature distribution in the riser pipe is shown in the contour diagrams. For the comparability of the experiments with the simulations, the diagrams for the simulations only contain the temperature data at the positions where a sensor is also present in the experiment. These positions are marked with black lines on the ordinate. The mass flow curves are shown in Fig. 8d. The unstable behavior in the experiment develops only from t = 8700 s. In the experiment, first three and then two separate mass flow peaks form per period. Also, the simulation with the modified model shows a separated peak structure with a more intense peak followed by a weaker one. Two peaks can also be seen in the standard model, but these are not as pronounced. The contour diagrams show that the temperature level during the warmup phase is higher in the simulations than in the experiment, which explains the early occurrence of the instabilities. Another striking feature is the prediction of the water that returns from the basin.

Figure 9 shows the results for geysering instability at maximum heating power and an aperture of 7 mm. The mass flow signals do not show any major differences between the two models. Compared to the experiment, the mass flow peak is overestimated in the simulation, and the simulations do not show any backflow in the downcomer. The increase in the mass flow, i.e., evaporation, also runs faster in the simulations. Comparing the contour plots, shortly after the mass flow peak in the modified model, like the experiment, the backflow at the condensation hit falls deeper into the riser than in the standard model. Since there is a backflow throughout the circuit during the experiment, the cold fluid stagnates in the riser pipe at times. Another difference can be seen during the outburst, where the standard model underestimates

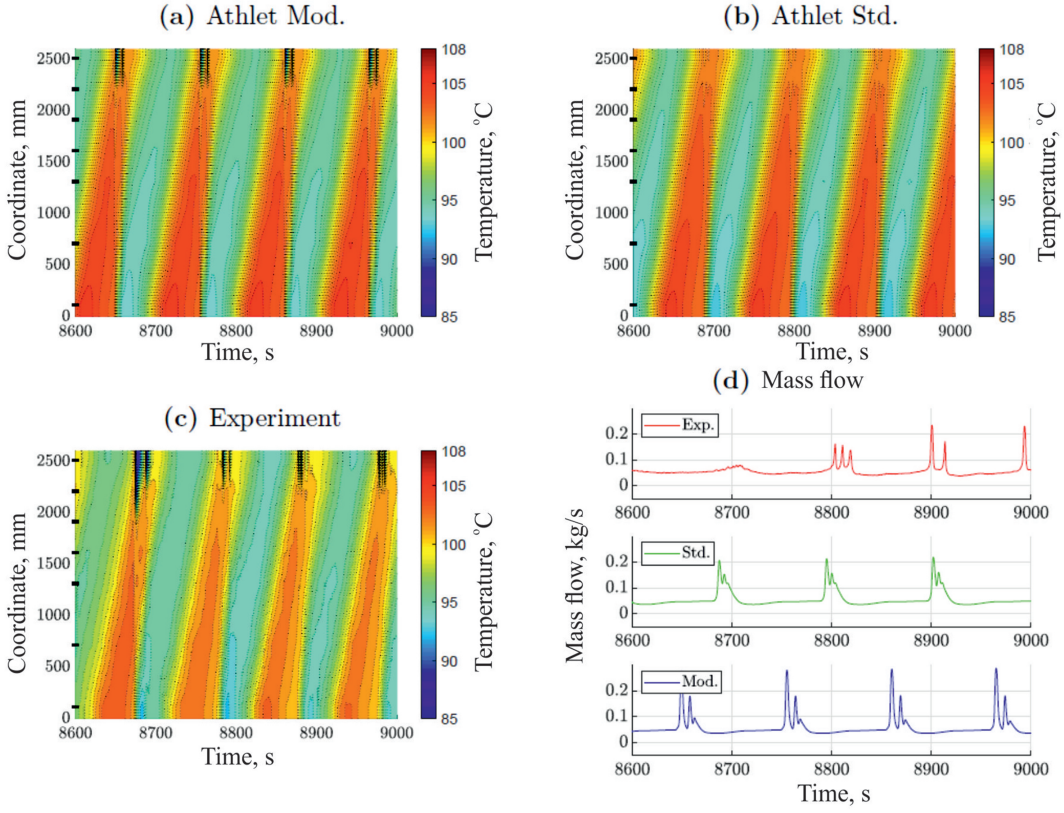

Fig. 8. Contour plots comparing simulation results of (a) modified evaporation model and (b) standard evaporation model with (c) experimental results and (d) mass flow rate for experiment with extended riser without choke at P_{rel} = 100%.

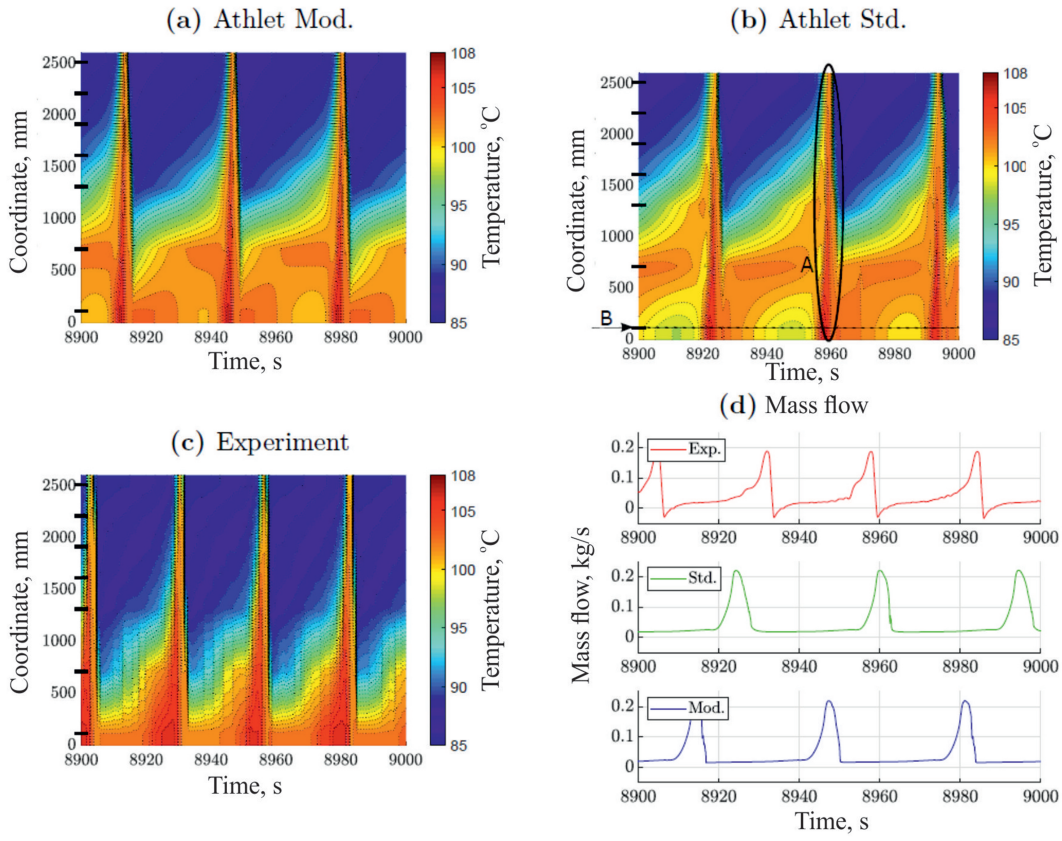

Fig. 9. Contour plots comparing simulation results of (a) modified evaporation model and (b) standard evaporation model with (c) experimental results and (d) mass flow rate for experiment with extended riser and 7-mm choke at P_{rel} = 100%.

the outburst duration and the fluid temperature (marker A). Furthermore, in the standard model, larger temperature fluctuations over time can be seen at the riser pipe inlet (marker B).

The characteristics summarized in Table I show better values for the modified evaporation model in this simulation. Especially, the integral mass flow shows very good results with the modified evaporation model.

From the results presented in Table I, no clear tendencies toward preference of the standard model or the modified evaporation model can be determined for the test cases simulated here. The standard model is advantageous for predicting the maximum mass flow peak. The modified evaporation model, on the other hand, predicts the frequency of the instabilities better, especially for geysering.

However, an undoubted advantage of geyser forecasting is applied in cases using a modified model; for example, for engineering calculations of natural circulation circuits where it is necessary to avoid pulsations and geysering or to predict them, to maintain the strength characteristics of pipes, collectors, and their connections.

Figure 10 shows the pressure curves for the tests from measurement campaign 2 without an aperture (Fig. 10a), with a 9-mm aperture (Fig. 10b), and with a 7-mm aperture (Fig. 10c) from the simulations of both evaporation models and the experimental results. Since the pressure sensors are read with f = 1000 Hz in the experiment, the frequency with which the data were written out during the simulations was set to 1000 Hz to detect the short-term pressure peaks to allow comparison of the data. A logarithmic ordinate was used here for a better representation of the entire pressure range.

For the operating point (Fig. 10a), both the simulations and the experiment show two consecutive peaks with decreasing amplitude. Both times the peaks are underestimated in the simulations, with the simulation using the modified model coming closer to the experiment. The constant pressure curve between the two peaks is also shown better here. However, both simulations do not show the small condensation shocks that occur in the experiment.

For the 9-mm aperture, only very small pressure peaks can be seen in the simulation with the standard evaporation model, whereas the pressure peaks with the modified evaporation model are around 1 bar. In the experiment, the

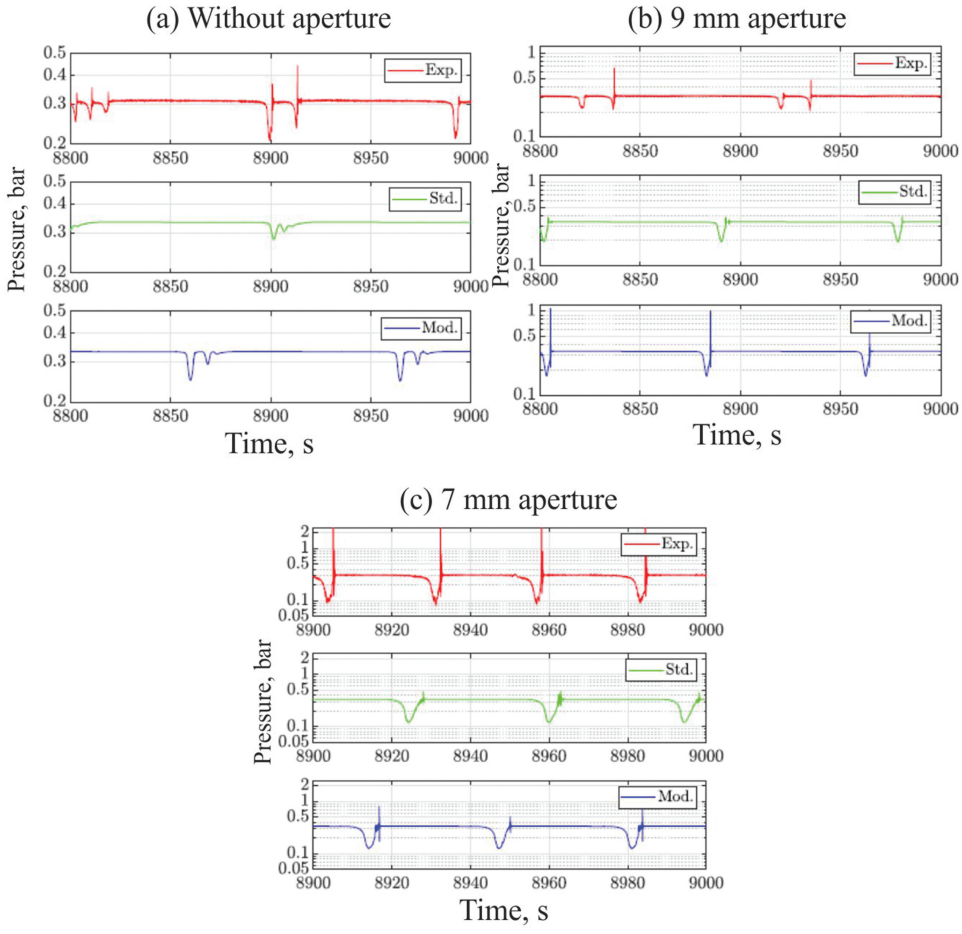

Fig. 10. Pressure curves during instabilities at P_{rel} = 100% for experiments from second measurement campaign. Exp. is experimental data, Std. is standard evaporation model, and Mod. is modified evaporation model.

pressure peaks are between 0.5 bar and 0.7 bar. However, it should be noted that during one period in the experiment, two separate peaks occur and so the discharge of the vapor is divided between them, which leads to smaller condensation hammers in the experiment. In case (c), where geysering occurs, the condensation hammers are again very small with the standard evaporation model. The modified evaporation model also shows higher pressure values of up to 0.8 bar here. In the experiment, the maximum measurable pressure of 2.5 bar is exceeded in this case. In summary, it can be said that, compared to the standard evaporation model, the simulations with the modified evaporation model were better able to predict the condensation hammers.

V. CONCLUSION

This paper discussed natural circulation modeling using the ATHLET system code. To this effect, a special INTRAVIT test facility was built at the University of Luxembourg to carry out tests at various thermal loads and various angles of the condenser tube from 5 to 90 deg. An analysis of the existing evaporation model in ATHLET showed that it is only a very simplified representation of the physical processes that occur. In the paper, along with an analysis of the literature on existing evaporation models, a modified evaporation model was proposed that offers a realistic description of various evaporation processes. It describes the onset of bubble formation using a nucleation model. In addition, a model for calculating the surface density was introduced, which is necessary for simulating evaporation.

In total, five different test configurations were created in ATHLET with the help of which several experiments that were simulated for stable and unstable natural circulation.

It was shown that the simulation results were in good agreement with the experimental data for stable natural circulation. For unstable natural circulation, the calculations of

the standard evaporation model and the modified evaporation model were compared. Based on the simulated test cases, it was not possible to determine a trend in favor of one of the two evaporation models. In terms of frequency determination, the modified evaporation model performed better, while the standard evaporation model was better at predicting the maximum mass flow rate of the instabilities. The simulation of the pressure peaks of the resulting condensation hammers was better calculated with the modified evaporation model.

Simulations with the one-dimensional system code ATHLET showed deviations for an accurate simulation of the instabilities with both the standard evaporation model and the modified evaporation model. To more accurately represent the nature of the transient three-dimensional flow structures, three-dimensional computational fluid dynamics codes could be used in the future. To validate these simulations, INTRAVIT, together with a possible integration of grid sensors, represents a suitable test facility.

Nomenclature

A_i = surface density (1/m)
a = thermal diffusivity (m^2/s)
C_d = drag coefficient
d = diameter (mm)
f = frequency (Hz)
g = gravity acceleration (m/s^2)
J = nucleation rate (1/m)
Ja = Jakob number
$\dot{m}$ = mass flow (kg/s)
Nu = Nusselt number
n = volume-specific number (1/m)
P = pressure (Pa)
Pr = Prandtl number
Re = Reynolds number
r = radius (mm)
T = temperature (K)
t = time (s)
W = velocity (m/s)

Subscripts and Superscripts

av = average
BL = boundary layer
b = bubble
c, crit = critical
det = detachment
f = fluid
fls = flashing
geys = geysering
h = hydraulic
NS = nucleation sites
rel = relative
st = steam
sup = superheated
w = wall

Greek

α = heat transfer coefficient (W/m^2K)
β = inclination angle (deg)
ζ = pressure loss coefficient
δ = thickness (mm)
λ = thermal conductivity (W/m·K)
θ = contact angle (deg)
μ = dynamic viscosity (Pa·s)
ε = volume vapor content
ν = cinematic viscosity (m^2/s)
ρ = density (kg/m^3)
σ = surface tension (Nm)

Credit Authorship Contribution Statement

Michel Haag: Conceptualization, formal analysis, investigation, data curation. I. Dolganov: Supervision, writing—original draft, writing—review and editing. Stephan Leyer: Project administration, supervision, funding acquisition.

Disclosure Statement

No potential conflict of interest was reported by the author(s).

ORCID

Iurii Dolganov http://orcid.org/0009-0000-2149-1214
Stephan Leyer http://orcid.org/0000-0003-4893-397X

References

1. G. LERCHL et al., *ATHLET 3.1A: User's Manual*, 1st ed., GRS gmbH (2016).
2. M. S. PLESSET and S. A. ZWICK, "The Growth of Vapor Bubbles in Superheated Liquids," *J. Appl. Phys.*, **25**, 493 (1954); http://dx.doi.org/10.1063/1.1721668.
3. M. BLANDER and J. KATZ, "Bubble Nucleation in Liquids," *AIChe J.*, **21**, *5*, 833 (1975); http://dx.doi.org/10.1002/aic.690210502.
4. R. COLE, "Boiling Nucleation," *Adv. Heat Transfer*, **10**, 85 (1974); http://dx.doi.org/10.1016/S0065-2717(08)70110-2.
5. R. COLE, "Bubble Frequencies and Departure Volumes at Subatmospheric Pressures," *AlChE J.*, **13**, *4*, 779 (1967); http://dx.doi.org/10.1002/aic.690130434.
6. V. P. SKRIPOV, R. KONDOR, and D. SLUTZKIN, *Metastable Liquids*, Wiley and Jerusalem and London: Israel Program for Scientific Translations (1974).
7. R. S. MILLER, "Photographic Observations of Bubble Formation in Flashing Nozzle Flow," *J. Heat Transfer*, **107**, *4*, 750 (1985); http://dx.doi.org/10.1115/1.3247500.
8. N. I. KOLEV, *Multiphase Flow Dynamics 3. Thermal Interactions*, 4th ed., Springer (2011); http://dx.doi.org/10.1007/978-3-642-21372-4.
9. J. R. RIZNIC and M. ISHII, "Bubble Number Density and Vapor Generation in Flashing Flow," *Int. J. Heat Mass Transfer*, **32**, *10*, 1821 (1989); http://dx.doi.org/10.1016/0017-9310(89)90154-3.
10. J. R. THOME, *Encyclopedia of Two-Phase Heat Transfer and Flow*, World Scientific (2015).
11. K. MISHIMA and M. ISHII, "Flow Regime Transition Criteria for Upward Two-Phase Flow in Vertical Tubes," *Int. J. Heat Mass Transfer*, **27**, *5*, 723 (1984); http://dx.doi.org/10.1016/j.net.2021.08.014.
12. T. S. SHIN and O. C. JONES, "Nucleation and Flashing in Nozzles. A Distributed Nucleation Model," *Int. J. Multiphase Flow*, **19**, *6*, 943 (1993); http://dx.doi.org/10.1016/0301-9322(93)90071-2.
13. N. BASU, G. R. WARRRIER, and V. K. DHIR, "Onset of Nucleate Boiling and Active Nucleation Site Density During Subcooled Flow Boiling," *ASME J. Heat Transfer*, **124**, *4*, 717 (2002); http://dx.doi.org/10.1115/1.1471522.
14. T. HIBIKI and M. ISHII, "Active Nucleation Site Density in Boiling Systems," *Int. J. Heat Mass Transfer*, **46**, *14*, 2587 (2003); http://dx.doi.org/10.1016/S0017-9310(03)00031-0.
15. N. ZUBER, "Nucleate Boiling. The Region of Isolated Bubbles and the Similarity with Natural Convection," *Int. J. Heat Mass Transfer*, **6**, *1*, 53 (1963); http://dx.doi.org/10.1016/0017-9310(63)90029-2.
16. M. ISHII and I. KATAOKA, "Interfacial Transfer in Annular Dispersed Flow," Argonne National Laboratory (1982); http://dx.doi.org/10.1007/978-94-009-6845-5_6.
17. A. CIONCOLINI and J. R. THOME, "Entrained Liquid Fraction Prediction in Adiabatic and Evaporating Annular Two-Phase Flow," *Nucl. Eng. Des.*, **243**, 200 (2012); http://dx.doi.org/10.1016/j.nucengdes.2011.11.014.
18. M. S. EL-GENK and H. H. SABER, "Minimum Thickness of a Flowing Down Liquid Film on a Vertical Surface," *Int. J. Heat Mass Transfer*, **44**, *15*, 2809 (2001); http://dx.doi.org/10.1016/S0017-310(00)00326-4.
19. P. DERGARABEDIAN, "The Rate of Growth of Vapor Bubbles in Superheated Water," *J. Appl. Mech.*, **20**, *4*, 537 (1953); http://dx.doi.org/10.1115/1.4010761.
20. A. A. AVDEEV, *Bubble Systems*, Springer Berlin (2016); http://dx.doi.org/10.1007/978-3-319-29288-5.
21. V. GNIELINSKI, "Neue Gleichungen für den Wärme- und den Stoffübergang in turbulent durchströmten Rohren und Kanälen," *Forsch. Ingenieurwes.*, **41**, 8 (1975); http://dx.doi.org/10.1007/BF02559682.
22. H. D. BAEHR and K. STEPHAN, *Heat and Mass Transfer*, 3rd rev. ed., Springer (2011).
23. K. LEE and D. J. RYLEY, "The Evaporation of Water Droplets in Superheated Steam," *Int. J Heat and Mass Trans.*, **78**, 445 (1968); http://dx.doi.org/10.1115/1.3597540.